

Design-Oriented Analysis and Performance Evaluation of Clamped-Current-Boost Input-Current Shaper for Universal-Input-Voltage Range

Laszlo Huber, *Member, IEEE*, and Milan M. Jovanović, *Senior Member, IEEE*

Abstract— In cost-sensitive off-line applications, compliance with the existing line-current harmonic standards can be achieved by employing clamped-current-boost (CCB) input-current shapers (ICS's). In this paper, a thorough analysis of the CCB ICS is presented, and a complete design-oriented mathematical model is derived. The design equations are given in closed forms so that they can be easily computed by any standard mathematical software. The model is verified experimentally on a 100-W universal-input-voltage-range ICS.

Index Terms— Boost ac-dc converter, clamped-current control, line-current shaper, power factor correction.

I. INTRODUCTION

AS IT HAS BEEN demonstrated in [1]–[4], various power-quality standards, such as IEC 1000-3-2 [5], can be met by line-current shapers that are substantially different from sinusoidal ones. A trapezoidal waveshaper is particularly attractive due to its potential to achieve high power factor (PF) with low peak-to-rms ratio (crest factor) and relatively low total harmonic distortion (THD) [1]. In [1]–[4], trapezoidal-waveshape approaches are exploited in implementing various simple low-cost boost input-current shapers (ICS's). These ICS's, also known as clamped-current-boost (CCB) ICS's [2]–[4], do not require dedicated ICS controllers. Instead, any conventional current-mode pulse-width-modulation (PWM) controller chip can be used to control the CCB ICS's.

The conceptual circuit diagram of the CCB ICS is shown in Fig. 1. In this circuit, the PWM modulator compares the difference between reference voltage V_{ref} and slope-compensation ramp v_R (used to stabilize the current loop for duty cycles $>50\%$) with the voltage on sensing resistor R_i , which is proportional to inductor current i_L . It should be noted that in the CCB ICS, reference voltage V_{ref} is not derived from the rectified line voltage, but it is equal to the output voltage of the error amplifier V_e . Since for ICS's the crossover frequency of the voltage-regulation loop is much lower than twice the line frequency (typically, four–eight times) [6], the output voltage of the error amplifier is practically constant during a half-line cycle. As a result, the peak inductor current is limited (clamped) by the constant reference V_{ref} , which makes the input current roughly trapezoidal. Note that in practical

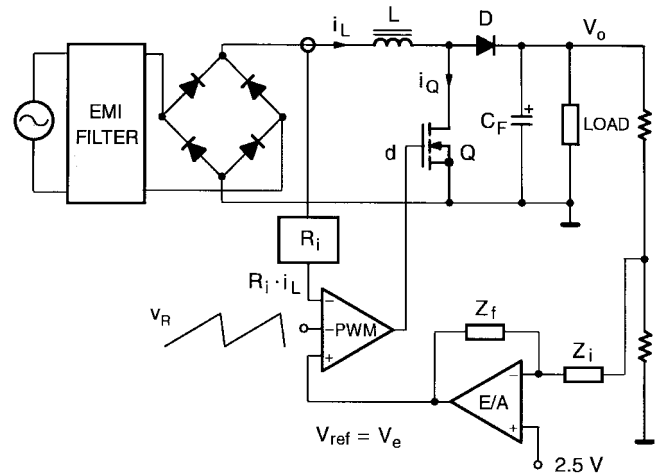


Fig. 1. Conceptual circuit diagram of CCB ICS.

circuits, sensing of inductor current i_L is implemented by sensing the switch current i_Q since during on-time $i_L = i_Q$.

So far, a number of papers have been published dealing with the analysis and design of the CCB ICS's. In [2], detailed analysis of the CCB ICS is performed for the circuit operating with maximum duty cycle ≤ 0.5 and without external ramp. A simplified analysis of and design guidelines for the CCB ICS operating with maximum duty cycle close to 100% and external ramp are presented in [3]. Finally, in [4], the average-current control scheme for the CCB ICS's is proposed.

The objective of this paper is to present a complete design-oriented analysis of the clamped-current control for CCB ICS's by extending the analysis given in [3] to include the effects of the boost inductance, switching frequency, and maximum duty cycle of the controller. The design equations that include all these effects are derived in closed forms so that they can easily be computed by any standard mathematical software, thus making it possible for design engineers to apply the given design equations to their own sets of design specifications. The presented mathematical model of and design procedure for the CCB ICS are experimentally verified on a universal input-voltage-range 100-W prototype converter.

II. ANALYSIS

In this section, the analysis of the CCB ICS shown in Fig. 1 is performed assuming the following.

Manuscript received February 12, 1997; revised September 15, 1997. Recommended by Associate Editor, K. D. T. Ngo.

The authors are with Delta Power Electronics Lab., Inc., Blacksburg, VA 24060 USA.

Publisher Item Identifier S 0885-8993(98)03344-4.

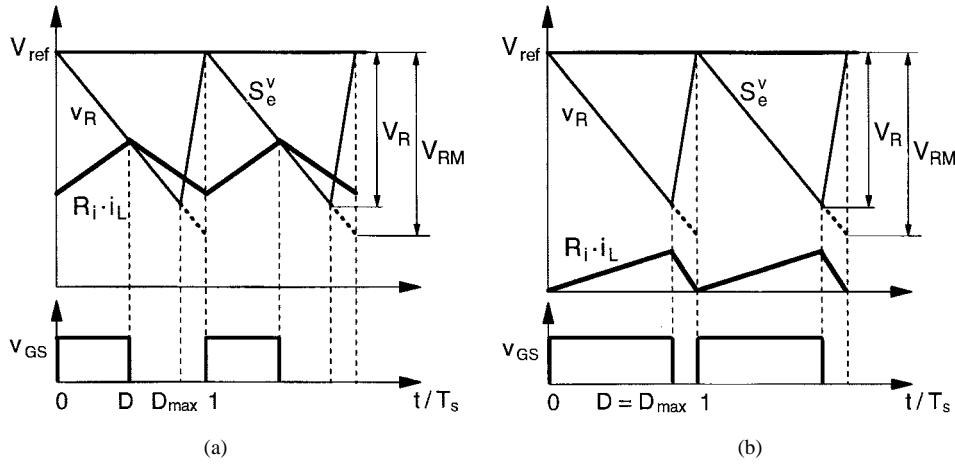


Fig. 2. Reference voltage V_{ref} , slope-compensation ramp v_R , sensed voltage $R_i \cdot i_L$, and duty cycle of CCB ICS: (a) switch turns off when $R_i \cdot i_L$ reaches $V_{ref} - v_R$, and (b) switch turns off when duty cycle D reaches D_{max} .

- 1) Input voltage is a full-wave-rectified sine wave, i.e., $v_i = V_{im} |\sin(\omega_L t)|$, where V_{im} is the amplitude and ω_L is the angular frequency.
- 2) The dc-output-voltage V_o has a negligible ac ripple.
- 3) Switching frequency f_s is constant and much larger than line frequency f_L , so that the input voltage can be considered constant during a switching cycle (quasi-static approach).
- 4) Reference voltage V_{ref} to the PWM modulator is constant during each half of a line cycle because the bandwidth of the output-voltage loop is much smaller than the rectified line frequency ($2f_L$).
- 5) Phase shift of the line current caused by the input filter can be neglected.

In the CCB ICS in Fig. 1, the conduction of switch Q is initiated by the internal oscillator of the controller (not shown in Fig. 1). The switch is turned off either when sensed voltage $R_i \cdot i_L$ reaches the difference between reference voltage $V_{ref} = V_e$ and slope-compensation-ramp voltage v_R , i.e.,

$$R_i i_L = V_{ref} - v_R \quad (1)$$

as shown in Fig. 2(a) or when the duty cycle of the switch reaches its preset maximum D_{max} , as illustrated in Fig. 2(b).

Within a half-line cycle, the boost inductor can operate in both the discontinuous-conduction mode (DCM) and continuous-conduction mode (CCM). At lower instantaneous line voltages, the boost-inductor current i_L is discontinuous, while at higher line voltages i_L is continuous. Depending on which event terminates the conduction of Q in a switching cycle, two discontinuous and two continuous conduction modes of operation are possible. In this paper, the DCM and CCM, where Q turns off when the switch duty ratio reaches D_{max} [Fig. 2(b)], are denoted as DCM1 and CCM1, respectively. Similarly, the DCM and CCM in which sensed voltage $R_i i_L$ reaches the difference voltage $V_{ref} - v_R$ [Fig. 2(a)] are denoted as DCM2 and CCM2, respectively. From the two CCM's, only CCM2 needs to be considered since CCM1 usually encom-

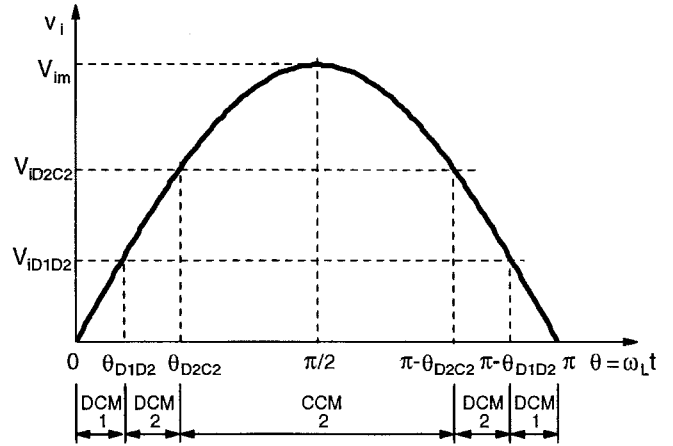


Fig. 3. The CCB ICS operation modes.

passes only a few switching cycles with fast rising or falling edges of the inductor current, which can be approximated with vertical segments, as illustrated in Fig. 6(a). The three operation modes within a half of a line cycle are shown in Fig. 3. Depending on the line and load conditions, three mode sequences (MS's) can be distinguished, as summarized in Table I.

In MS1, there is a direct transition from DCM1 to CCM2. In DCM1 ($D = D_{max}$), the peak-sensed voltage $R_i i_L$ is always smaller than the difference of reference voltage V_{ref} and peak slope-compensation-ramp voltage V_R [see Fig. 2(b)]. MS3 is without DCM1, i.e., the peak-sensed voltage always reaches the difference of the reference voltage and the slope-compensation-ramp voltage $V_{ref} - v_R$. By inspection of Fig. 2(b), it can be easily found that the condition for MS3 is $V_{ref} - V_R \leq 0$. Finally, MS2 is the MS between MS1 and MS3.

Expressions of the inductor current waveforms in the three operation modes as well as expressions for the boundary angles between the operation modes are derived next. Since it is more convenient to perform these derivations by using current signals instead of voltage signals, reference current I_{ref} and

TABLE I
CCB ICS MS'S

MODE SEQUENCE	OPERATION MODE			MS CONDITION	BOUNDARY ANGLE	
	DCM1	DCM2	CCM2		θ_{DD}	θ_{DC}
MS1	+		+	$V_{ref} - V_R > R_L i_{L,pk,DCM1,max}$ (See Eq. (14))	θ_{D1C2}	θ_{D1C2}
MS2	+	+	+	$0 < V_{ref} - V_R < R_L i_{L,pk,DCM1,max}$	θ_{D1D2}	θ_{D2C2}
MS3		+	+	$V_{ref} - V_R < 0$	0	θ_{D2C2}

slope-compensation-ramp current i_R are defined from (1) as

$$i_L = \frac{V_{ref}}{R_i} - \frac{v_R}{R_i} = I_{ref} - i_R. \quad (2)$$

To obtain the expressions for inductor current waveforms and boundary angles, the slope of the compensation ramp must be determined first.

A. Slope-Compensation Ramp

To ensure the stability of the current loop, the slope of the compensation (external) ramp S_e^i should be at least 50% of the maximum down slope of the inductor current in CCM2 $S_{f,max}^i$, i.e.,

$$S_e^i = k_S \cdot S_{f,max}^i, \quad k_S \geq 0.5. \quad (3)$$

From Fig. 2(a) and (2), the slope of the compensation ramp is

$$S_e^i = \frac{I_R}{D_{max}T_s} = \frac{I_{RM}}{T_s}. \quad (4)$$

The inductor current in CCM2 has a maximum down slope at the DCM1-CCM2 boundary

$$S_{f,max}^i = \frac{V_o - V_{iD1C2}}{L} \quad (5)$$

where the input voltage at the DCM1-CCM2 boundary is

$$V_{iD1C2} = (1 - D_{max}) \cdot V_o. \quad (6)$$

Substituting (6) into (5) and using (3), the slope of the compensation ramp is determined as

$$S_e^i = k_S \cdot \frac{D_{max}V_o}{L}. \quad (7)$$

Finally, from (4) and (7), the amplitude of the compensation ramp $I_{RM} = V_{RM}/R_i$ is obtained as

$$I_{RM} = k_S \cdot \frac{D_{max}V_o}{Lf_s} \quad (8)$$

where $f_s = 1/T_s$,

B. Discontinuous Conduction Mode

In DCM, the average inductor current, which is also the line current, is defined as

$$i_{L,ave,DCM} = \frac{T_{on} + T'_{off}}{2T_s} \cdot i_{L,pk,DCM} \quad (9)$$

where T'_{off} is the time which it takes for the inductor current to decrease from $i_{L,pk,DCM}$ to zero and $i_{L,pk,DCM}$ is the peak inductor current

$$i_{L,pk,DCM} = \frac{V_{im}|\sin(\omega_L t)|}{Lf_s} \cdot D_{DCM} \quad (10)$$

where $D_{DCM} = T_{on}/T_s$. T'_{off} is determined from the inductor flux balance as

$$T'_{off} = \frac{V_{im}|\sin(\omega_L t)|}{V_o - V_{im}|\sin(\omega_L t)|} \cdot T_{on}. \quad (11)$$

Substituting (10) and (11) into (9), the average inductor current in DCM is obtained as

$$i_{L,ave,DCM} = \frac{1}{2Lf_s} \cdot \frac{V_{im}|\sin(\omega_L t)|}{1 - \frac{V_{im}|\sin(\omega_L t)|}{V_o}} \cdot D_{DCM}^2. \quad (12)$$

In DCM1, $D_{DCM} = D_{max}$ and (12) becomes

$$i_{L,ave,DCM1} = \frac{1}{2Lf_s} \cdot \frac{V_{im}|\sin(\omega_L t)|}{1 - \frac{V_{im}|\sin(\omega_L t)|}{V_o}} \cdot D_{max}^2. \quad (13)$$

It should be noted that at low line voltages $V_{im}|\sin(\omega_L t)| \ll V_o$, the average inductor current in DCM1 is proportional to the line voltage.

The maximum value of the peak inductor current in DCM1, which determines the condition for MS1, is obtained by setting $D_{DCM} = D_{max}$ and by substituting (6) for the instantaneous rectified line voltage $V_{im}|\sin(\omega_L t)|$ in (10)

$$i_{L,pk,DCM1,max} = \frac{D_{max}(1 - D_{max})V_o}{Lf_s}. \quad (14)$$

In DCM2, the inductor current reaches the difference of the reference current and ramp current, i.e.,

$$i_{L,pk,DCM2} = I_{ref} - I_{RM}D_{DCM2}. \quad (15)$$

From (10) and (15)

$$D_{DCM2} = \frac{I_{ref}}{I_{RM} + \frac{V_{im}|\sin(\omega_L t)|}{Lf_s}} \quad (16)$$

and substituting (16) into (12), the average inductor current in DCM2 is obtained as

$$i_{L,ave,DCM2} = \frac{1}{2Lf_s} \cdot \left(\frac{I_{ref}}{I_{RM}} \right)^2 \cdot \frac{V_{im}|\sin(\omega_L t)|}{\left(1 - \frac{V_{im}|\sin(\omega_L t)|}{V_o} \right) \cdot \left(1 + \frac{V_{im}|\sin(\omega_L t)|}{I_{RM}Lf_s} \right)^2}. \quad (17)$$

Again, at low line voltages, $V_{im}|\sin(\omega_L t)| \ll V_o$ and $V_{im}|\sin(\omega_L t)| \ll I_{RM}Lf_s = k_S D_{max} V_o$ [according to (8)], and the average inductor current in DCM2 is proportional to the line voltage.

C. Continuous Conduction Mode

In CCM2, the average inductor current is defined as

$$i_{L,ave,CCM2} = i_{L,pk,CCM2} - \frac{\Delta i_{L,CCM2}}{2} \quad (18)$$

where

$$i_{L,pk,CCM2} = I_{ref} - I_{RM}D_{CCM2} \quad (19)$$

is the peak inductor current and $\Delta i_{L,CCM2}$ is the peak-to-peak inductor-current ripple

$$\Delta i_{L,CCM2} = \frac{V_{im}|\sin(\omega_L t)|}{Lf_s} \cdot D_{CCM2}. \quad (20)$$

From the inductor flux balance, the switch duty ratio is determined as

$$D_{CCM2} = 1 - \frac{V_{im}|\sin(\omega_L t)|}{V_o}. \quad (21)$$

Substituting (19)–(21) into (18), the average inductor current in CCM2 is obtained as

$$i_{L,ave,CCM2} = I_{ref} - I_{RM} + \left(\frac{I_{RM}}{V_o} - \frac{1}{2Lf_s} \right) V_{im}|\sin(\omega_L t)| + \frac{V_{im}^2}{2Lf_s V_o} \sin^2(\omega_L t). \quad (22)$$

It can be seen from (22) that the average inductor current in CCM2 consists of three components: a constant-current component, a component proportional to the line voltage (desired component), and a component proportional to the square of the line voltage. The three CCM2 current components are shown in Fig. 4.

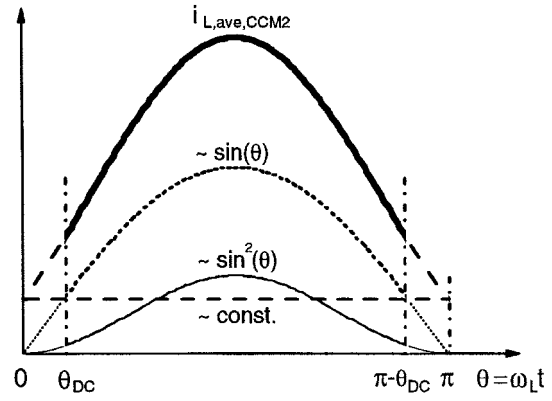


Fig. 4. Current components in CCM2.

To make the desired component which is proportional to line voltage positive, from (8) and (22) it follows that it is necessary to satisfy the condition

$$k_S > \frac{1}{2D_{max}}. \quad (23)$$

Similarly, from (8) and (22), the ratio of the amplitudes of the desired component and the component proportional to the square of the line voltage is equal to

$$\frac{V_o}{V_{im}}(2k_S D_{max} - 1). \quad (24)$$

From (24), it can be seen that a larger external ramp increases the amplitude of the desired component. Also, according to (24), with increasing V_{im} , the contribution of the component proportional to the square of the line voltage to the total average inductor current increases. It should be noted that the sign of the constant-current component can be positive or negative depending on the input voltage and output power.

D. Boundary Angle Between Operation Modes

The DCM1-DCM2 boundary angle is obtained from (10) and (15) at $D_{DCM} = D_{max}$

$$\theta_{D1D2} = a \sin \left[\frac{Lf_s}{V_{im}} \left(\frac{I_{ref}}{D_{max}} - I_{RM} \right) \right] \quad (25)$$

while the DCM1-CCM2 boundary angle is directly determined from (6)

$$\theta_{D1C2} = a \sin \left(\frac{V_o}{V_{im}}(1 - D_{max}) \right). \quad (26)$$

Finally, the DCM2-CCM2 boundary angle θ_{D2C2} is obtained by equating the peak inductor current from (19) with the peak-to-peak inductor-current ripple from (20), and using (21)

$$I_{ref} = I_{RM} \left(1 + \frac{V_{im} \sin(\theta_{D2C2})}{I_{RM}Lf_s} \right) \cdot \left(1 - \frac{V_{im} \sin(\theta_{D2C2})}{V_o} \right). \quad (27)$$

E. Reference Current

The reference current in (17), (22), (25), and (27) can be determined from the input-output power balance

$$P_i = \frac{2}{\pi} V_{im} \left(\int_0^{\theta_{DD}} i_{L,ave,DCM1}(\theta) \sin(\theta) d(\theta) + \int_{\theta_{DD}}^{\theta_{DC}} i_{L,ave,DCM2}(\theta) \sin(\theta) d(\theta) + \int_{\theta_{DC}}^{\pi/2} i_{L,ave,CCM2}(\theta) \sin(\theta) d(\theta) \right) = \frac{P_o}{\eta} \quad (28)$$

where $\theta = \omega_L t$ and η is the efficiency of the ICS power stage. Equation (28) encompasses all three MS's from Table I. The definition of boundary angles θ_{DD} and θ_{DC} is given in Table I.

The input power during CCM2 can be expressed in a closed form. By substituting (22) into (28), after integration it follows:

$$P_{i,CCM2} = \frac{2}{\pi} V_{im} (I_{ref} - I_{RM}) \cos(\theta_{DC}) + \frac{1}{\pi} V_{im}^2 \left(\frac{I_{RM}}{V_o} - \frac{1}{2Lf_s} \right) \cdot \left(\frac{\pi}{2} - \theta_{DC} + \frac{\sin(2\theta_{DC})}{2} \right) + \frac{1}{3\pi} \frac{V_{im}^3}{Lf_s V_o} \cos(\theta_{DC}) (2 + \sin^2(\theta_{DC})). \quad (29)$$

The input power during DCM1 and DCM2 can be obtained by numerical integration of the following:

$$P_{i,DCM1} = \frac{1}{\pi} \frac{V_{im}^2 D_{max}^2}{Lf_s} \int_0^{\theta_{DD}} \frac{\sin^2(\theta)}{1 - \frac{V_{im} \sin(\theta)}{V_o}} d\theta \quad (30)$$

and

$$P_{i,DCM2} = \frac{1}{\pi} \frac{V_{im}^2}{Lf_s} \left(\frac{I_{ref}}{I_{RM}} \right)^2 \cdot \int_{\theta_{DD}}^{\theta_{DC}} \frac{\sin^2(\theta)}{\left(1 - \frac{V_{im} \sin(\theta)}{V_o} \right) \cdot \left(1 + \frac{V_{im} \sin(\theta)}{I_{RM} Lf_s} \right)^2} d\theta. \quad (31)$$

In MS1, the boundary angles are equal, $\theta_{DD} = \theta_{DC} = \theta_{D1C2}$, and, as can be seen from (26), independent of the reference current. Hence, by substituting θ_{D1C2} from (26) into (29) and (30), I_{ref} can be directly determined from the power balance (28).

In MS3, the boundary angles are $\theta_{DD} = 0$ and $\theta_{DC} = \theta_{D2C2}$, defined by (27). After substituting I_{ref} from (27) into (29) and (31), from the power balance (28) the boundary angle θ_{D2C2} can be found first. Then, I_{ref} can be calculated from (27).

Finally, in MS2, the boundary angles are $\theta_{DD} = \theta_{D1D2}$ (25) and $\theta_{DC} = \theta_{D2C2}$ (27). Again, after replacing I_{ref} from (27) into (25) and (29)–(31), from the power balance (28) the

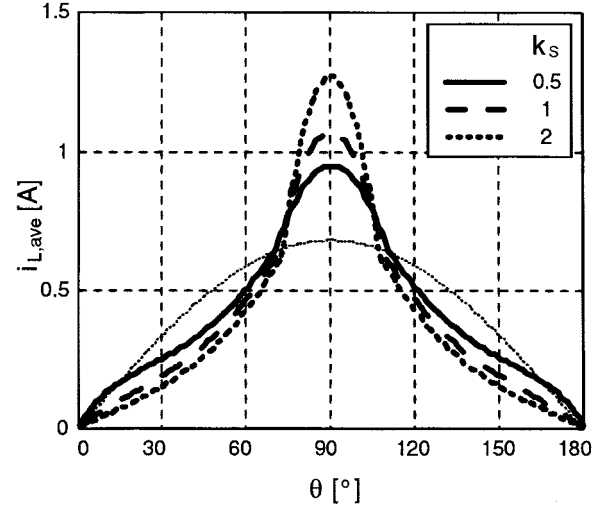


Fig. 5. Line-current waveform versus k_S at $V_{i,rms} = 230$ V.

TABLE II
PF AND THD VERSUS k_S AT $V_{i,rms} = 230$ V

k_S	PF	THD [%]
0.5	0.971	24.4
1	0.942	35.7
2	0.898	49.1

boundary angle θ_{D2C2} can be found first, and then I_{ref} can be calculated from (27).

The whole procedure described above can be easily implemented by using any standard mathematical software (e.g., Mathcad). In a particular design, I_{ref} is calculated for all three MS's. The actual value of I_{ref} , i.e., the actual MS, is the one which satisfies one MS condition from Table I.

F. Input-Current Harmonics

The input current contains only odd harmonics whose rms value can be determined by using Fourier analysis

$$I_{i,k} = \frac{2\sqrt{2}}{\pi} \left(\int_0^{\theta_{DD}} i_{L,ave,DCM1}(\theta) \sin(k\theta) d(\theta) + \int_{\theta_{DD}}^{\theta_{DC}} i_{L,ave,DCM2}(\theta) \sin(k\theta) d(\theta) + \int_{\theta_{DC}}^{\pi/2} i_{L,ave,CCM2}(\theta) \sin(k\theta) d(\theta) \right). \quad (32)$$

The THD is obtained by summing up the squares of the first N (e.g., $N = 19$) odd harmonics

$$THD = \frac{\sqrt{\sum_k I_{i,k}^2}}{I_{i,1}}, \quad k = 3, 5, \dots, (2N + 1). \quad (33)$$

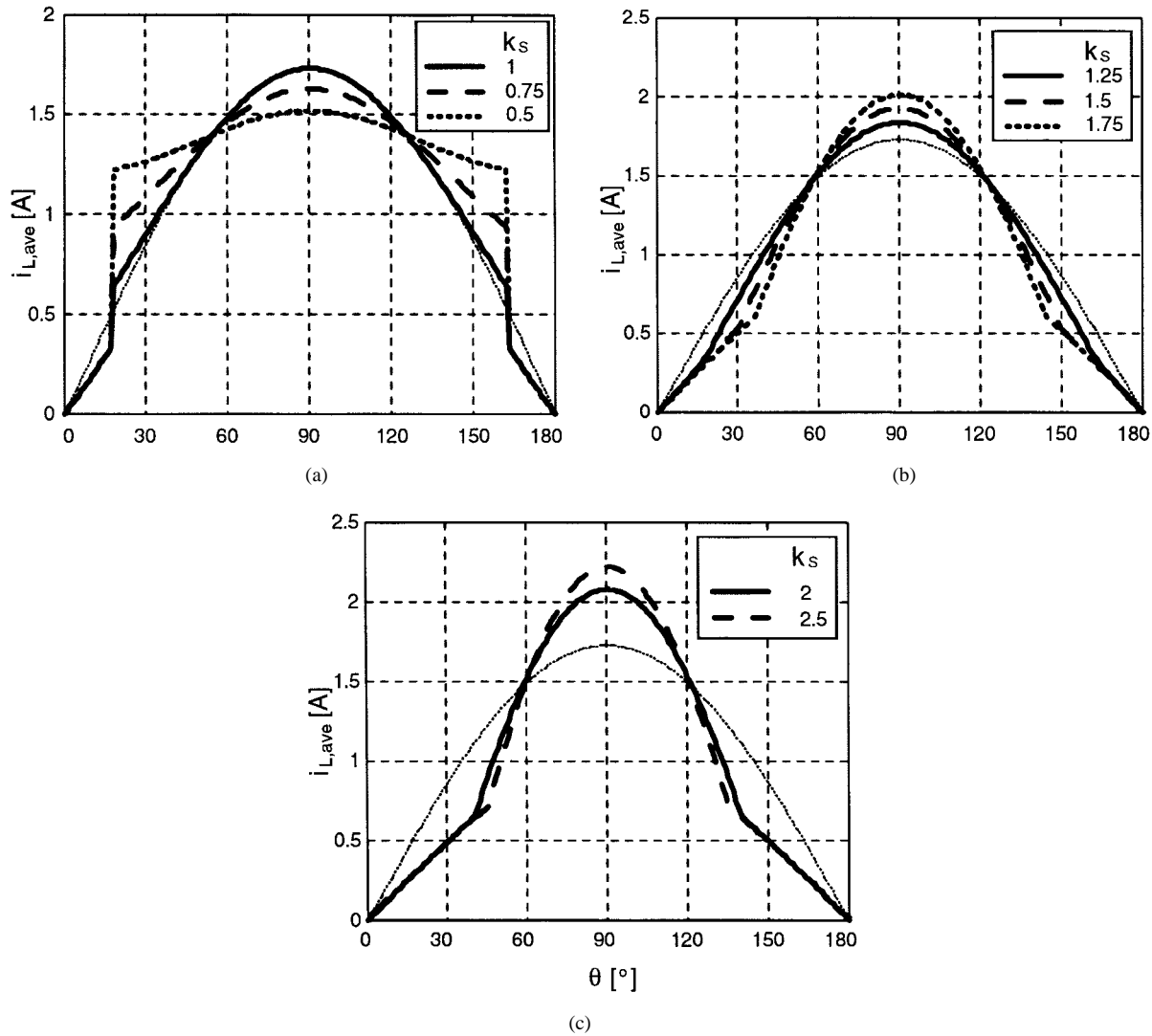


Fig. 6. Line-current waveform versus k_S at $V_{i,rms} = 90$ V in (a) MS1, (b) MS2, and (c) MS3.

III. DESIGN

In this section, the derived mathematical model is used in the design of an experimental 100-W/385-Vdc CCB ICS for the universal input-voltage range ($V_{i,rms} = 90\text{--}265$ V).

According to the line-current components, determined by (13), (17), and (22), the design variables are the product of boost inductance L and switching frequency f_s , maximum duty cycle D_{max} , and the height of the ramp current, I_{RM} . The design of Lf_s and D_{max} is determined by the specifications of the power stage and performed as for a conventional boost ICS circuit [6]. Therefore, the design of the CCB ICS in this paper is focused on the control circuit, particularly on the ramp current height I_{RM} determined by (8). The key design parameter is the normalized slope of the ramp current k_S .

For higher line voltages, i.e., $V_{i,rms} > 180$ V, the operation corresponds to MS3. In MS3, the quality of the line current is inversely proportional to k_S , i.e., with increasing k_S , PF decreases and THD increases. As an example, line-current waveforms obtained in Mathcad for three different values of k_S at $V_{i,rms} = 230$ V ($L = 0.5$ mH, $f_s = 100$

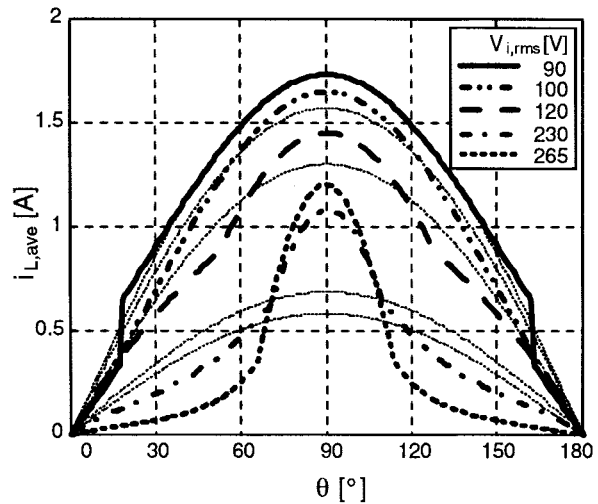


Fig. 7. CCB ICS line-current waveform versus $V_{i,rms}$ with $k_S = 1$ at full load. Ideal sinusoidal line-current waveforms are also shown (...).

kHz, $D_{max} = 0.9$, and $\eta = 0.9$) are shown in Fig. 5—the corresponding values of PF and THD (calculated for the first

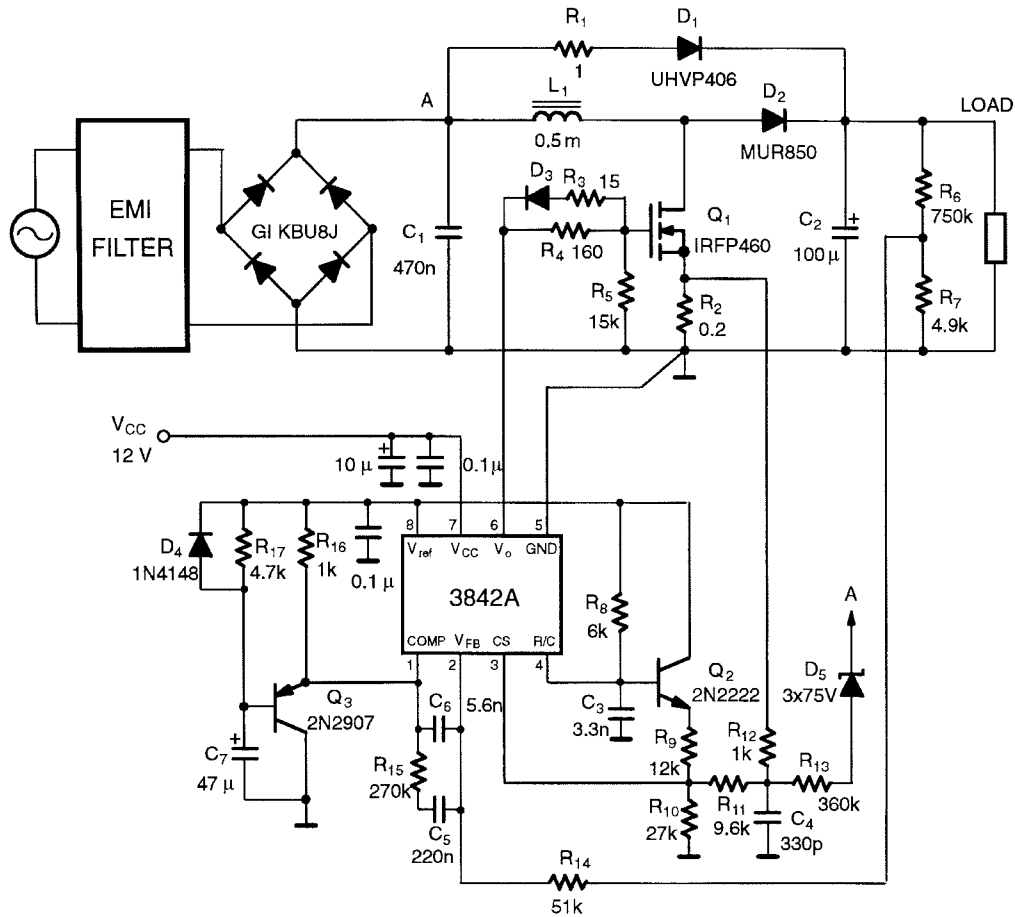


Fig. 8. Experimental CCB ICS circuit diagram.

19 odd harmonics) are given in Table II.

At lower line voltages, all three MS's are possible. For example, at minimum line voltage $V_{i,rms} = 90$ V, with increasing k_S the operation changes from MS1 \rightarrow MS2 \rightarrow MS3, as presented in Table III and Fig. 6. In MS2, similarly as in MS3, the quality of the line current is inversely proportional to k_S , i.e., with increasing k_S , PF decreases and THD increases. However, in MS1, the quality of the line current varies proportionally to k_S , i.e., with increasing k_S , PF increases and THD decreases. It was found to be a good design compromise to select k_S so that at minimum line voltage, operation in MS1 close to the boundary with MS2 is achieved. It follows from Table III that $k_S = 1$.

Line-current waveforms obtained in Mathcad with $L = 0.5$ mH, $f_s = 100$ kHz, $D_{max} = 0.9$, $\eta = 0.9$, and $k_S = 1$ for five rms line voltages are shown in Fig. 7. The circuit operates in MS1 at $V_{i,rms} = 90$ V, in MS2 at $V_{i,rms} = 100$ V and $V_{i,rms} = 120$ V, and in MS3 at $V_{i,rms} = 230$ V and $V_{i,rms} = 265$ V. Corresponding values of PF and THD are given in Table IV. The values of I_{ref} and boundary angles θ_{DD} and θ_{DC} are also included in Table IV. In Figs. 5–7, ideal sinusoidal line-current waveforms are also shown.

It should be noted that the line-current waveform and PF at higher line voltages can be improved by employing nonlinear feedforward control [3].

TABLE III
MS, PF, AND THD VERSUS k_S AT $V_{i,rms} = 90$ V

k_S	MS	PF	THD [%]
0.5	1	0.98	20.4
0.75	1	0.993	11.6
1	1	0.999	4.3
1.25	2	0.997	8.2
1.5	2	0.99	14.4
1.75	2	0.983	18.6
2	3	0.977	21.9
2.5	3	0.965	27.0

The experimental circuit diagram is shown in Fig. 8. The control circuit is based on the conventional current-mode PWM controller 3842 [7]. Design of resistors R_2 , R_9 , R_{10} , and R_{11} which are related to the external ramp is given in [8].

IV. EXPERIMENTAL RESULTS

Experimental line-current waveforms at full resistive load ($I_{LOAD} = 0.26$ A) for four rms line voltages are presented in Fig. 9(a)–(c) and (e). The experimental waveforms are in good agreement with the theoretical waveforms, except for

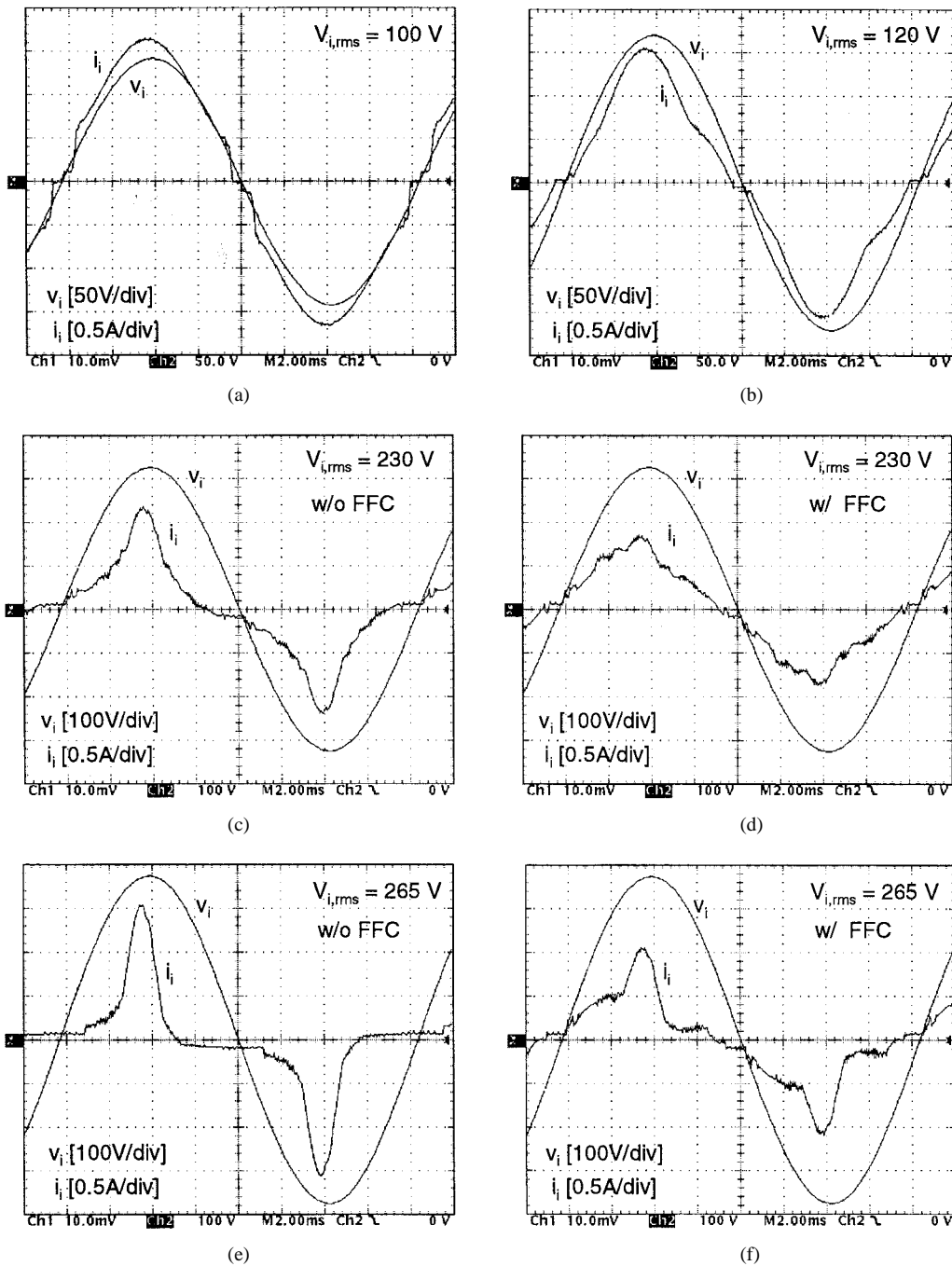


Fig. 9. Experimental line voltage and current waveforms at full resistive load ($V_o = 385$ V and $I_o = 0.26$ A).

TABLE IV
BASIC CHARACTERISTICS at $k_S = 1$ ($I_R = 6.24$ A,
 $I_{RM} = 6.93$ A, $\Delta i_{L,pk,DCM1,max} = 0.693$ A)

$V_{i,rms}$ [V]	MS	I_{ref} [A]	θ_{DD} [°]	θ_{DC} [°]	PF	THD [%]
90	1	7.22	18	18	0.999	4.3
100	2	6.93	16	16	0.998	5.7
120	2	6.27	1	52	0.995	9.8
230	3	2.66	0	71	0.942	35.7
265	3	1.49	0	66	0.825	68.2

the additional phase shift in the experimental line-current waveforms, which is due to the effect of the input filter.

In order to improve the quality of the line-current waveform at higher rms line voltages, i.e., to increase PF and decrease THD, feedforward control [3] is employed at $v_i(t) > 225$ V. The nonlinear feedforward control is implemented with three 75-V Zener diodes in series, as shown in Fig. 8. Instead of high-voltage Zener diodes, low-voltage Zener diodes can be used with an additional resistive voltage divider. Notice that at lower rms line voltages ($V_{i,rms} = 100$ V and $V_{i,rms} = 120$ V), the feedforward control has no effect, i.e., the Zener diode D_5 in Fig. 8 is never conducting. As can be seen from Fig. 9(d) and (f), the feedforward limits the peak current and makes

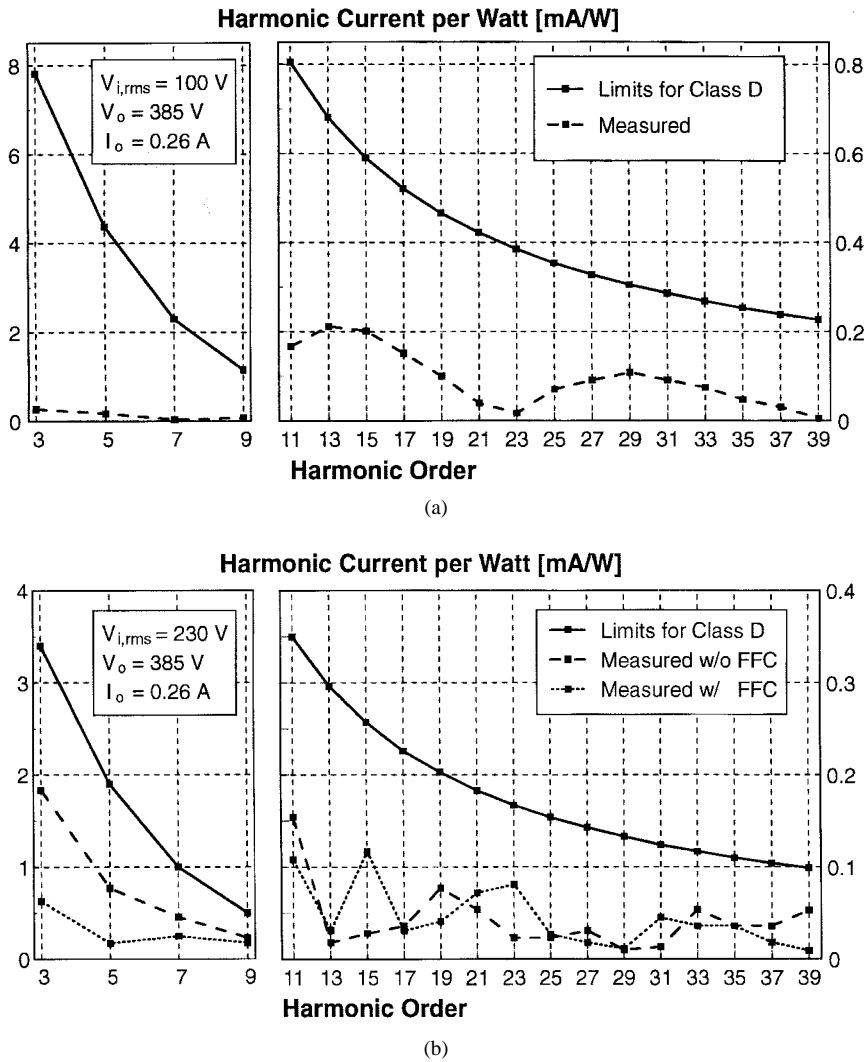


Fig. 10. Experimental line-current harmonics at full resistive load at (a) $V_{i,rms} = 100$ V and (b) $V_{i,rms} = 230$ V with and without feedforward control (FFC).

the current waveform wider, resulting in higher PF and lower THD. The measured PF and THD for five rms line voltages are presented in Table V. The measured line-current harmonics at $V_{i,rms} = 100$ V and $V_{i,rms} = 230$ V are shown in Fig. 10. The harmonic limits for Class D from the IEC 1000-3-2 standard [5] are also given in Fig. 10. The limits for $V_{i,rms} = 100$ V are obtained by multiplying the $V_{i,rms} = 230$ V limits with $230/100 = 2.3$. As can be seen from Fig. 10, the measured harmonics are well below the limits. It should be noted that the IEC 1000-3-2 specifications are satisfied even without the implementation of the feedforward control.

At higher rms line voltages, the line current contains some irregularities which can be explained with the circuit behavior in DCM. Namely, after the boost diode turns off, the MOSFET drain-source capacitance and the boost diode capacitance oscillate with the boost inductance, as shown in the inductor-current waveforms in Fig. 11. The amount of charge transferred back into the filter capacitance C_1 varies depending on the duration of DCM. For example, in Fig. 11(c), the DCM oscillation consists of three half sinusoids, which means that more charge is transferred into C_1 than out of C_1 , i.e., extra charge is available from C_1 to supply the load and less charge has to be

TABLE V
MEASURED PF AND THD VERSUS $V_{i,rms}$
WITHOUT AND WITH FEEDFORWARD CONTROL

$V_{i,rms}$ [V]	w/o FFC		w/ FFC	
	PF	THD [%]	PF	THD [%]
90	0.994	10.4	0.994	10.4
100	0.996	5.6	0.996	5.6
120	0.979	18.1	0.979	18.1
230	0.876	45.9	0.954	17.3
265	0.706	90.0	0.851	44.2

drawn from the line. Hence, the line current slightly decreases around interval T_2 . In DCM around interval T_3 , there are two full-sinusoidal oscillations, and no extra charge is accumulated in C_1 , resulting in no distortion of the line current. Around interval T_1 , the circuit operates in CCM. The irregularities in the line-current waveform at higher line voltages can be made smaller by increasing the filter capacitance C_1 .

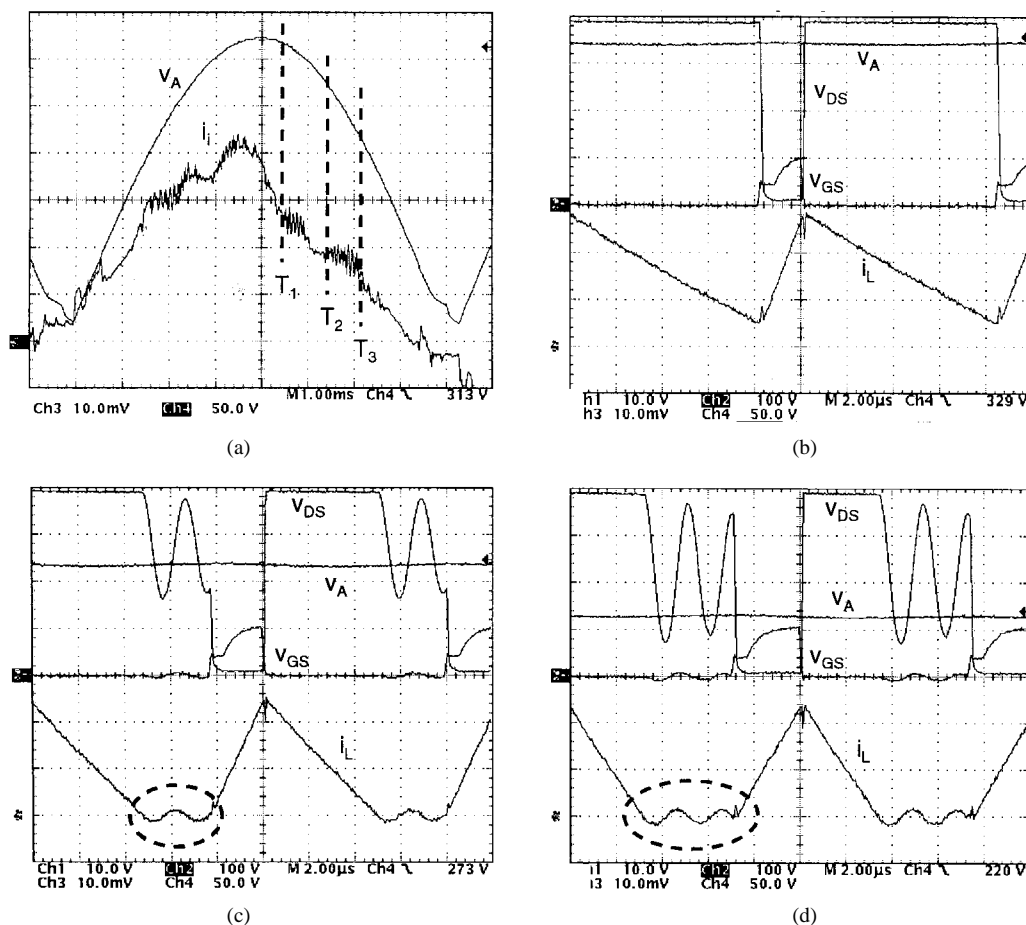


Fig. 11. Line-current waveform irregularities at $V_{L,rms} = 230$ V with feedforward control. (a) Line current [0.2 A/div] and rectified line voltage [50 V/div] waveforms—expanded waveforms around intervals (b) T_1 , (c) T_2 , and (d) T_3 ; v_{DS} [100 V/div], v_A [50 V/div], v_{GS} [10 V/div], and i_L [0.5 A/div].

V. SUMMARY

A design-oriented analysis of the CCB ICS that includes the effects of the boost inductance, switching frequency, and maximum duty cycle of the controller is presented. The derived design equations are given in closed forms so that they can easily be computed by any standard mathematical software. The presented mathematical model of and proposed design procedure for the CCB ICS are experimentally verified on a universal-input-voltage-range 100-W converter. It is demonstrated that the CCB ICS meets the IEC 1000-3-2 standards.

REFERENCES

- [1] N. J. Barabas, "Simplified control algorithm for active power factor correction," in *Power Conversion Int. (PCI) Conf. Proc.*, Oct. 1985, pp. 1–9.
- [2] D. Maksimović, "Design of the clamped-current high-power-factor boost rectifier," in *IEEE Applied Power Electronics Conf. (APEC) Proc.*, Feb. 1994, pp. 584–590.
- [3] R. Redl and B. R. Erisman, "Low-cost power-factor correction/line-harmonics reduction with current-clamped boost converter," in *Power Conversion Proc.*, June 1995, pp. 229–239.
- [4] R. Redl, A. S. Kislovski, and B. P. Erisman, "Input-current clamping: An inexpensive novel control technique to achieve compliance with harmonic regulations," in *IEEE Applied Power Electronics Conf. (APEC) Proc.*, Mar. 1996, pp. 145–151.
- [5] "Electromagnetic compatibility (EMC)—Part 3: Limits—Section 2: Limits for harmonic current emissions (equipment input current ≤ 16 A per phase)," IEC 1000-3-2 Document, 1st ed., 1995.
- [6] L. H. Dixon, Jr., "High power factor preregulators for off-line power supplies," *Unitrode Switching Regulated Power Supply Design Seminar Manual*, Paper I2, SEM-700, Unitrode Integrated Circuits, Merrimack, NH, 1990.
- [7] *Product & Application Handbook*, Unitrode Integrated Circuits, Merrimack, NH, 1995–1996.
- [8] L. Huber and M. M. Jovanović, "Analysis, design, and performance evaluation of clamped-current boost input-current shaper for universal input-voltage-range applications," in *High Frequency Power Conversion Conf. (HFPC) Proc.*, Sept. 1996, pp. 41–51.

Laszlo Huber (M'86), for a photograph and biography, see this issue, p. 486.

Milan M. Jovanović (S'86–M'89–SM'89), for a photograph and biography, see this issue, p. 486.